

Fe Site Order and Magnetic Properties of $\text{Fe}_{1/4}\text{NbS}_2$

Erick A. Lawrence, Xudong Huai, Dongwook Kim, Maxim Avdeev, Yu Chen, Grigorii Skorupskii, Akira Miura, Austin Ferrenti, Moritz Waibel, Shogo Kawaguchi, Nicholas Ng, Bobby Kaman, Zijian Cai, Leslie Schoop, Satya Kushwaha, Feng Liu, Thao T. Tran, and Huiwen Ji*

Cite This: *Inorg. Chem.* 2023, 62, 18179–18188

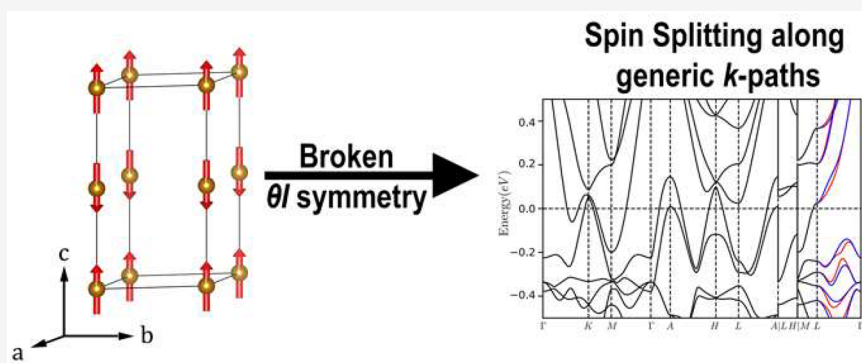
Read Online

ACCESS |

Metrics & More

Article Recommendations

Supporting Information



ABSTRACT: Transition-metal dichalcogenides (TMDs) have long been attractive to researchers for their diverse properties and high degree of tunability. Most recently, interest in magnetically intercalated TMDs has resurged due to their potential applications in spintronic devices. While certain compositions featuring the absence of inversion symmetry such as $\text{Fe}_{1/3}\text{NbS}_2$ and $\text{Cr}_{1/3}\text{NbS}_2$ have garnered the most attention, the diverse compositional space afforded through the host matrix composition as well as intercalant identity and concentration is large and remains relatively underexplored. Here, we report the magnetic ground state of $\text{Fe}_{1/4}\text{NbS}_2$ that was determined from low-temperature neutron powder diffraction as an A-type antiferromagnet. Despite the presence of overall inversion symmetry, the pristine compound manifests spin polarization induced by the antiferromagnetic order at generic k points, based on density functional theory band-structure calculations. Furthermore, by combining synchrotron diffraction, pair distribution function, and magnetic susceptibility measurements, we find that the magnetic properties of $\text{Fe}_{1/4}\text{NbS}_2$ are sensitive to the Fe site order, which can be tuned via electrochemical lithiation and thermal history.

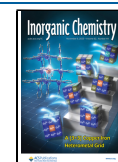
INTRODUCTION

Transition-metal dichalcogenides (TMDs) have long been the focus of significant scientific interest for their fascinating physical properties, including superconductivity,^{1,2} charge-density waves,^{3–6} nontrivial topological phases,^{7–9} etc. Crystallizing in layered structures, many possibilities arise from the van der Waals (vdW) gap between layers,^{10,11} such as the intercalation of a guest species, which is a powerful tool for manipulating the electronic, thermal, optical, and magnetic properties of TMDs^{12–17} and is a facile process driven by charge transfer from guest species to the host framework.^{18,19} Intercalating magnetic atoms, such as Fe, Cr, Ni, Mn, and Co, causes TMDs to develop long-range magnetic order upon cooling below their respective transition temperatures.^{20–25} Intercalation is performed through solid-state synthesis or a novel metal carbonyl route.^{26,27} Stable superlattices due to unique ordering of the magnetic atoms are most commonly encountered at two intercalant concentrations [x per formula unit (f.u.) of TMD]: a centrosymmetric $2a \times 2a$ superlattice at

$x = 1/4$ and a noncentrosymmetric $\sqrt{3}a \times \sqrt{3}a$ lattice at $x = 1/3$.

Among magnetic-intercalated TMDs, Fe- and Cr-intercalated species at $x = 1/3$ received rejuvenated interest for their lack of inversion symmetry, resulting in intriguing properties suitable for spintronic applications, including electrical switching and chiral helimagnetism.^{28–31} Electrical switching of the antiferromagnetic (AFM) order for low-energy, swift information encoding and decoding was recently demonstrated in $\text{Fe}_{1/3}\text{NbS}_2$ (space group $P6_322$) below its Néel temperature (42 K),^{29,32,33} making the system one of a handful AFM candidates that demonstrated such low-power switching

Received: July 31, 2023
Revised: October 5, 2023
Accepted: October 6, 2023
Published: October 20, 2023



capability due to relativistic spin polarization by global or local centrosymmetry breaking such as CuMnAs³² and Mn₂Au.³³ Both in-plane stripe and zigzag-type ground states were found by neutron diffraction to coexist in Fe_{1/3}NbS₂, and their relative dominance depends on the sign of Fe off-stoichiometry.³⁴ In these materials, it is generally accepted that the Ruderman–Kittel–Kasuya–Yosida (RKKY) interaction is the dominant exchange mechanism that gives rise to magnetic ordering.^{35–37} Due to the oscillatory nature of the RKKY interaction as well as the triangular Fe sublattice, the site order of magnetic atoms determines the interatomic distance and thus exchange interaction sign and strength. Therefore, small Fe off-stoichiometry and site disorder might give rise to some degree of magnetic frustration to form a spin glass that is thought to play a crucial role in low-current-density switching characteristics.²⁹ Likewise, the unique spin canting and field-controllable helical magnetic states in Cr_{1/3}NbS₂ and Cr_{1/3}TaS₂ also originate from inversion symmetry breaking due to $\sqrt{3} \times \sqrt{3}$ Cr order, which enables the so-called Dzyaloshinskii–Moriya effect.^{31,38,39}

By contrast, magnetically intercalated TMDs at $x = 1/4$ are still relatively underexplored due to the conventional consensus that it is unwise to explore spin polarization for spintronic applications in materials that preserve inversion symmetry. However, recent theoretical works predicted spin polarization even in the overall centrosymmetric AFM compounds provided that certain structural and magnetic symmetries are preserved or broken.^{40,41} Evaluation of spin polarization in such centrosymmetric AFM compounds requires the magnetic structures of the target materials to be known. Compared to Fe_{1/3}NbS₂, Fe_{1/4}NbS₂ also has a much higher (and thus more practical) Néel temperature at ~ 150 K, which is strongly composition-dependent and quickly drops at Fe off-stoichiometry.^{21,42} Such a variation in the magnetic ordering temperature depending on the superlattice type was also observed in ferromagnetic analogues Fe_{1/4}TaS₂ and Fe_{1/3}TaS₂^{28,43} as well as Mn_{1/4}NbS₂ and Mn_{1/3}NbS₂.⁴⁴

In this paper, we present the AFM ground-state structure of Fe_{1/4}NbS₂ as determined by low-temperature neutron diffraction. Despite the presence of overall inversion symmetry, the pristine compound manifests spin polarization induced by the AFM order at generic k points, based on density functional theory (DFT) band-structure calculations. Furthermore, we investigate the electrochemical intercalation of magnetically inactive Li ions into Fe_{1/4}NbS₂ and find that lithiation is a facile method to incorporate ($\sqrt{3} \times \sqrt{3}$)-type Fe-ordering domains that coexist with the host (2×2)-type Fe-ordering domains, the proportion of which varies as a function of the degree of lithiation. Finally, we demonstrate the thermal-history effects on Fe site order using pair distribution function (PDF) analysis. Combining magnetic susceptibility measurements, we determine that the overall phase fraction of each Fe ordering type determines the relative dominance of the magnetic feature expressed at the respective Néel temperatures.

METHODS

No uncommon hazards are noted.

Synthesis. Fe_{1/4}NbS₂ was synthesized via a solid-state reaction. Stoichiometric Fe (99.9%, Sigma), Nb (99.8%, Sigma), and S (99.99%, Sigma) were ground in an agate mortar and pestle before pellets were pressed and sealed inside fused quartz ampules. The ampules were heated to 430 °C (1 °C/min) and held for 1 week to

allow the S vapor to sufficiently react before ramping to 900 °C (1 °C/min) for 48 h. Pristine slow-cooled and quenched samples were then prepared by pressing pellets of the as-synthesized powder, wrapping them in gold foil, and sealing them in evacuated fused quartz ampules. Slow-cooled samples were annealed at 300 °C for 18 h before being cooled at 0.5 °C/min to room temperature. Quenched samples were annealed at 400 °C for 18 h before being water-quenched. Single crystals were grown via chemical vapor transport by vacuum sealing 1 g of as-synthesized Fe_{1/4}NbS₂ in a 1.8-cm-diameter and 20-cm-long quartz tube with 2.2 mg/cm³ iodine as a vapor transport agent. Growth occurred for 2 weeks in a Lindberg Blue 3-zone furnace with the source set to 950 °C and the sink set to 800 °C.

Lithiated powder samples were prepared by pressing ~ 40 mg pellets of as-synthesized Fe_{1/4}NbS₂ powder, which were then assembled in coin cells (CR2032) using stainless steel cathode and anode caps, springs, glass microfiber filters (Whatman), 1 M LiPF₆ in an ethylene carbonate/dimethyl carbonate (DMC) solution (1:1, Sigma-Aldrich), and lithium foil (Sigma) that had been polished on both sides. Cells were assembled in an argon glovebox (MBraun) using a coin-cell crimper (Wellcos) and rested for 6 h before being discharged galvanostatically at 0.2 mA/g until they had reached the desired Li content (Arbin battery cycler, 25 °C). Cells were then disassembled, and the lithiated Li_xFe_{1/4}NbS₂ pellets were recovered, crushed, and washed twice with DMC (99+% extra dry, Acros Organics) to remove electrolyte salts. The lithiated powder was then homogenized to allow interdiffusion between Li and Fe by annealing following the procedures outlined in the above section for “slow-cooled” and “quenched” samples, respectively. Lithiation of single crystals was similarly performed.

Structure and Composition Determination. Neutron powder diffraction data were collected at 3, 125, 150, and 175 K on the high-resolution powder diffractometer Echidna at the Australian Nuclear Science and Technology Organization.⁴⁵ The measurements were done with neutrons of a wavelength of 2.4395 Å on the powder sample of ~ 1 g contained in a cylindrical vanadium can. Synchrotron X-ray diffraction (XRD) and PDF data were collected at the XU13 beamline with Lambda 750 K detectors in SPring-8. The wavelength was 0.206684 Å. The powder sample was packed into a quartz glass capillary of 0.3 mm diameter in an argon-filled glovebox. Rietveld refinement of neutron and synchrotron powder diffraction was performed using the GSAS code⁴⁶ with *EXPGUI* front-end.⁴⁷ Synchrotron powder diffraction data were converted to PDF data using the *xPDF*⁴⁸ suite. PDF refinement was performed using the *PDFGUI*⁴⁹ software package.

To determine the particle size and morphology, scanning electron microscopy (SEM) and electron-dispersive X-ray spectroscopy (EDS) were carried out at the University of Utah Nanofab Surface Analysis Lab. SEM imaging was performed using an FEI Quanta 600F scanning electron microscope at 20 kV, and EDS mapping was performed using an FEI Teneo equipped with an EDAX Octane Elite SDD detector at 14 kV.

Inductively coupled plasma mass spectrometry (ICP-MS) was performed by Galbraith Laboratories Inc. to determine the chemical stoichiometry using 200 mg of as-synthesized Fe_{1/4}NbS₂.

DFT Calculations. First-principles calculations were performed using DFT within the Vienna Ab initio Simulation Package (*VASP*).⁵⁰ Specifically, the Perdew–Burke–Ernzerhof-type generalized gradient approximation⁵¹ was employed for the exchange–correlation functional. The energy cutoff for the plane-wave basis was set to 260 eV, and the k -point sample was done with a $12 \times 12 \times 4$ Monkhorst–Pack⁵² grid. Experimentally determined lattice constants were used, and the atomic coordinates were fully relaxed with an energy threshold of 1×10^{-3} eV. The resultant band-structure calculations shown in the main text were compared with the computationally optimized lattice ($a = 6.66$ Å and $c = 11.70$ Å) and those under strains, which are shown in the [Supporting Information](#).

Magnetic Measurements. Field-cooled (FC) and zero-field-cooled (ZFC) direct-current (DC) magnetic susceptibility measurements were performed on Li_xFe_{0.25}NbS₂ using a vibrating-sample magnetometer option of either a Quantum Design Physical Properties

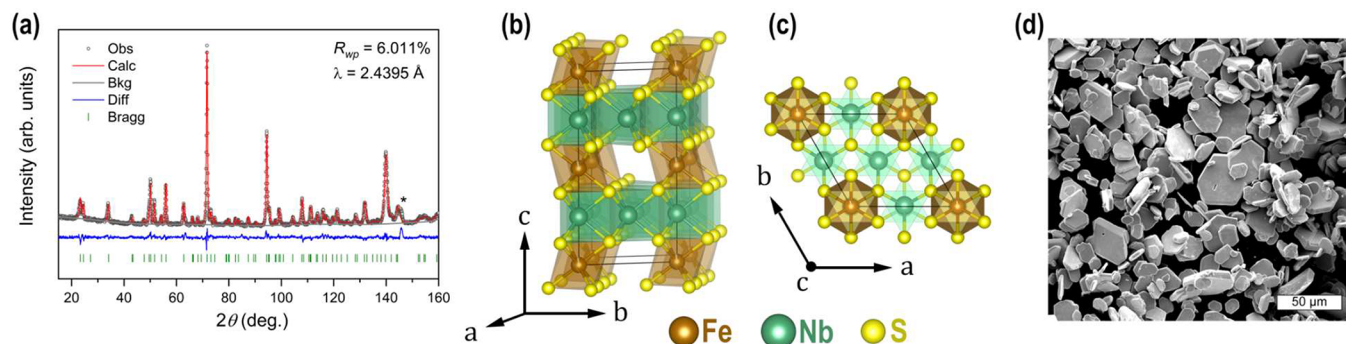


Figure 1. (a) Refinement of constant-wavelength powder neutron diffraction data collected at 175 K on pristine slow-cooled $\text{Fe}_{1/4}\text{NbS}_2$. An impurity peak at 145° is marked with an asterisk. Schematic views of the crystallographic structure of $\text{Fe}_{1/4}\text{NbS}_2$ along the (b) isometric view and (c) c axis. (d) SEM micrograph of the as-prepared powder.

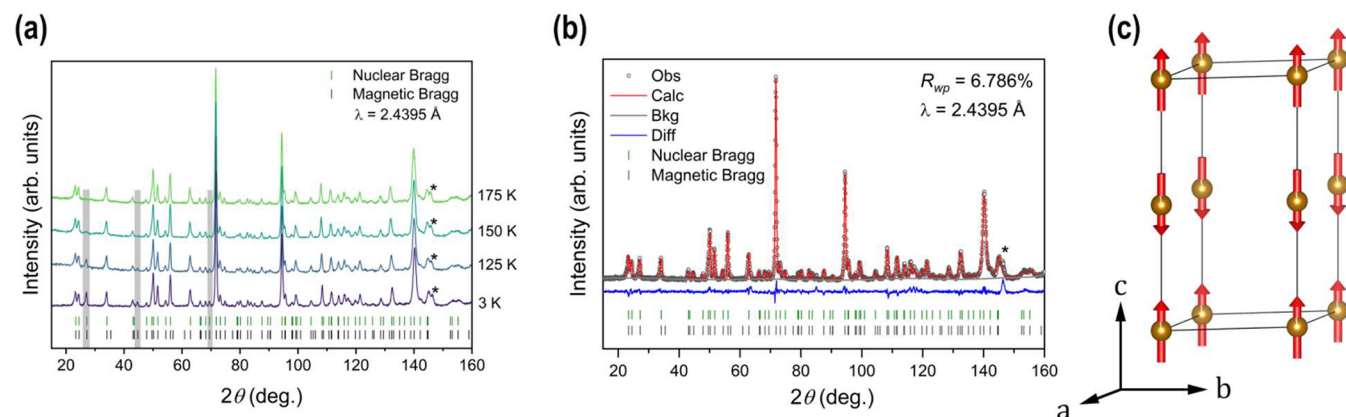


Figure 2. (a) Neutron diffraction of pristine slow-cooled $\text{Fe}_{1/4}\text{NbS}_2$ tracking the evolution of diffraction peaks from magnetic ordering as the sample is cooled from 175 to 3 K. The magnetic peaks evolve in the regions highlighted in gray, and the impurity peak at 145° is marked with an asterisk. (b) Refinement of powder neutron data collected at 3 K on pristine $\text{Fe}_{1/4}\text{NbS}_2$. The impurity peak at 145° is marked with an asterisk. (c) Schematic of the A-type AFM structure of $\text{Fe}_{1/4}\text{NbS}_2$.

Measurement System (PPMS) [$x = 0$ -SlowCool, 0.02, 0.04, 0.08] or a Magnetic Property Measurement System (MPMS) [single crystals, $x = 0$ -Quench, 0.01, 0.06, 0.09, 0.14]. Magnetic susceptibility was approximated as magnetization divided by the applied magnetic field: $\chi \approx M/H$. Alternating-current (AC) magnetization was measured using the ACMS option on a PPMS. Magnetization versus field measurements were performed using an MPMS.

RESULTS AND DISCUSSION

Synthesis and Magnetic Ground State of $\text{Fe}_{1/4}\text{NbS}_2$

The synthesis of polycrystalline $\text{Fe}_{1/4}\text{NbS}_2$ was performed through a solid-state reaction of stoichiometric precursors in an evacuated quartz ampule. The powder was annealed at 300°C and slowly cooled to room temperature. To verify the purity of the as-prepared phase, constant-wavelength neutron powder diffraction data were collected at 175 K in the paramagnetic state. The diffraction pattern and its Rietveld refinement are shown in Figure 1a, and the associated fit parameters are listed in Table S1. The refinement shows good agreement between the structural model and the diffraction data except for a minor unknown impurity peak at $\sim 145^\circ$ present at all temperatures. This impurity peak is not present in synchrotron diffraction. Crystal structure schematics viewed perpendicular to and along the c axis are shown in Figure 1b,c.

According to the structural model based on MnNb_4S_8 ,⁵³ Fe atoms do not randomly occupy all octahedral sites in the vdW gap but instead appear in every other site along the a and b

axes, resulting in a 2×2 superstructure of the base NbS_2 unit cell and retention of the overall hexagonal symmetry. Unlike its noncentrosymmetric analogue $\text{Fe}_{1/3}\text{NbS}_2$, $\text{Fe}_{1/4}\text{NbS}_2$ is centrosymmetric and each Fe site can be considered as an inversion center. The as-prepared $\text{Fe}_{1/4}\text{NbS}_2$ powder forms hexagonal platelets tens of microns in diameter, as shown in the SEM image in Figure 1d. The Fe content was refined and is slightly understoichiometric with $\sim 4\%$ Fe deficiency, resulting in a chemical formula of $\text{Fe}_{0.240(2)}\text{NbS}_2$.

ICP-MS was performed to independently verify the phase composition, yielding 8.24 wt % Fe, 53.0 wt % Nb, and 36.21 wt % S, which correspond to a chemical formula of $\text{Fe}_{0.26}\text{NbS}_2$. Both diffraction and ICP-MS methods confirm that the Fe content in the synthesized powder is very close to that of $\text{Fe}_{1/4}\text{NbS}_2$.

The magnetic ground state of $\text{Fe}_{1/4}\text{NbS}_2$ was studied by neutron diffraction at temperatures above and below the Néel temperature to observe the evolution of the diffraction peaks resulting from magnetic ordering (Figure 2a). Multiple peaks at 27° , 44.7° , and 69.5° emerge or become significantly more intense upon lowering of the temperature. Rietveld refinement was performed on the 3K data because the magnetic diffraction peaks were best pronounced. By starting with the nuclear space group ($P6_3/mmc$), magnetic subgroups obtained through k -SUBGROUPMAG⁵⁴ were sampled from high to low symmetry until all of the magnetic and nuclear diffraction peaks were indexed. Subsequent refinement based on viable

magnetic subgroups yielded a good fit with $R_w = 6.786\%$ based on $P6_3'/m'm'c$. The magnetic structure refinement statistics are comparable to the nuclear phase refinement; once again, the impurity peak at 145° is again the major cause of deviation between the calculation and actual data. The refinement is shown in Figure 2b, and the associated fit parameters are presented in Table S2.

The refinement of the 3K data revealed that the Fe moments in $\text{Fe}_{1/4}\text{NbS}_2$ order in an A-type collinear AFM structure (Figure 2c), with a ferromagnetic interaction within the plane and an AFM interaction across the layers. In this structure, the c axis is the easy axis, which is consistent with the literature⁴² and agrees with in-plane and out-of-plane DC magnetic susceptibility measurements performed on a lightly lithiated single-crystal sample of $\text{Li}_{0.01}\text{Fe}_{1/4}\text{NbS}_2$ (Figure S1), of which as we show later in the text, and the magnetic properties remain almost the same as pristine $\text{Fe}_{1/4}\text{NbS}_2$. The neutron-diffraction-derived magnetic moment is $3.51(4) \mu_B/\text{Fe}$, which is close to the expected $\sim 4 \mu_B/\text{Fe}$ -ordered magnetic moment given by $g \cdot S^{55}$ and based on the high-spin state of $S = 2$ for Fe^{2+} (the expected oxidation state of Fe in this structure³⁶). The values of the magnetic moments in Fe compounds are commonly lower than expected due to unsaturated moments.⁵⁶

The presence of centrosymmetry in $\text{Fe}_{1/4}\text{NbS}_2$ precludes the spin–orbit-coupling (SOC)-induced Rashba effect and spin polarization, which arise in the noncentrosymmetric $\text{Fe}_{1/3}\text{NbS}_2$. Meanwhile, the local site inversion asymmetry originates from the nonmagnetic NbS_6 triangular prisms, not the magnetic Fe layers, which cannot lead to the staggered current-induced fields that couple strongly with the magnetic layers like in CuMnAs .³² However, motivated by a recently proposed new scheme of realizing spin polarization in centrosymmetric compounds without SOC,^{41,57} we still explored k -dependent spin splitting in $\text{Fe}_{1/4}\text{NbS}_2$ using DFT band-structure calculations. The calculations first confirmed that the A-type AFM structure (regardless of magnetic anisotropy) is the ground state (Table S3). Based on previous predictions,^{41,57} an AFM structure that breaks the combination of time reversal (θ) and spatial inversion (I) and whose magnetic space group is either of the I or III type, as defined by Bradley and Cracknell,⁵⁸ will exhibit AFM-induced spin splitting despite global or local centrosymmetry. The two criteria are fulfilled in the A-type AFM structure of $\text{Fe}_{1/4}\text{NbS}_2$ solved from neutron diffraction, which breaks the θI symmetry with the alternating spins across layers and adopts a type III magnetic space group. The band structures with and without SOC based on the experimentally obtained lattice constants are shown in Figure 3. Although the bands are spin-degenerate along high-symmetry k paths, spin polarization was observed along a more generic k path (represented as a black solid line) along Γ – L , where the red and blue solid lines represent the opposite spin bands (Figure 3a). With SOC, the degeneracy is lifted, in contrast to the case without SOC (Figure 3b). Without SOC, the band degeneracy is protected along high-symmetry paths. Band-structure calculations based on computationally optimized lattice constants or under strain are shown in Figure S2 with similar observations. This compound therefore constitutes one example that manifests the new nonrelativistic spin-polarization effect classified as “altermagnetic”, where the spin splitting is induced by AFM instead of SOC.⁵⁹ Such nonrelativistic spin splitting can, depending on the symmetry, potentially lead to macroscopic responses such as an anomalous Hall effect, giant magneto-

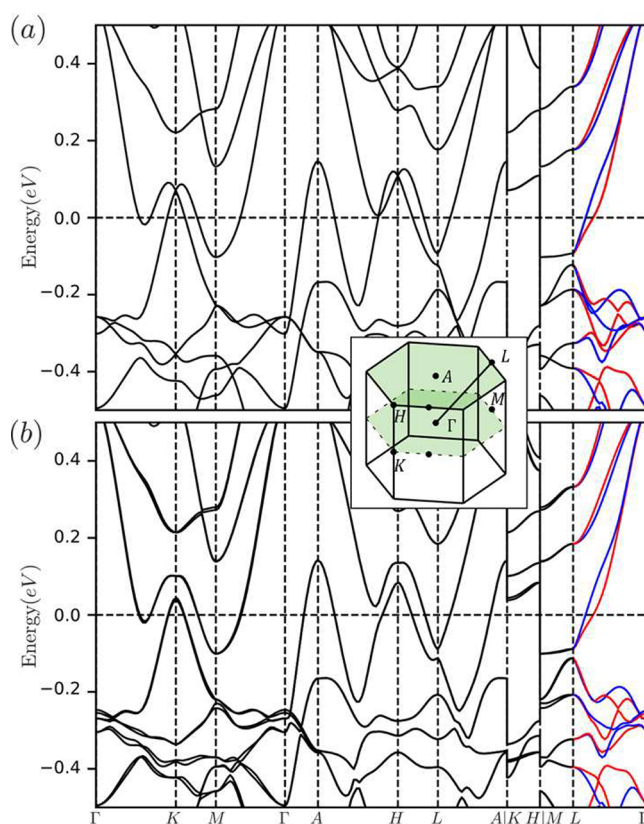


Figure 3. Spin-projected band structure of $\text{Fe}_{1/4}\text{NbS}_2$ (a) without and (b) with SOC. Red and blue lines represent the opposite spin components. When SOC is included, the S_z projected spin is considered. The degenerate bands with compensated spin components are plotted as black solid lines. The first Brillouin zone is included as an inset.

resistance, tunneling magnetoresistance, and spin–orbit torque.^{57,59}

Lithiation-Tuned Magnetic Interaction and Domain Structures.

Fe off-stoichiometry in $\text{Fe}_{1/3}\text{NbS}_2$ was previously associated with the rise of a spin glass phase, and an Fe-deficient composition $\text{Fe}_{0.31}\text{NbS}_2$ showed more pronounced electrical switching than an Fe-excess composition,⁶⁰ suggesting that subtle yet critical spin alignment resulted from Fe ordering in $\text{Fe}_{1/3-\delta}\text{NbS}_2$. Motivated by this observation, to explore the possible intermediate Fe ordering between $\text{Fe}_{1/4}\text{NbS}_2$ and $\text{Fe}_{1/3}\text{NbS}_2$, we applied lithiation to continuously modify the number of intercalants per f.u. $1/4 + x$ (x is the Li content) from $x = 0$ to 0.08. Note that, when $x = 0.08$, the number of intercalants with Fe and Li combined reaches $1/3$ per f.u. just like in $\text{Fe}_{1/3}\text{NbS}_2$ (voltage profiles of electrochemical lithiation are presented in Figure S3). Lithiation of functional materials often leads to modifications in physical properties, such as large changes in electrical conductivity,⁶¹ increased thermoelectric ZT score,⁶² a possible Anderson-localization-induced metal–insulator transition,⁶³ and temperature-independent magnetic behavior⁶⁴ to name a few. In this vein, we introduce Li^+ to act as a magnetically inert spacer in the vdW gap between NbS_2 slabs to tune the intercalant order and Fe–Fe distance in-plane with electrostatic interactions. Because Fe–Fe RKKY interaction oscillates with the distance, lithiation is expected to modify their magnetic interactions.

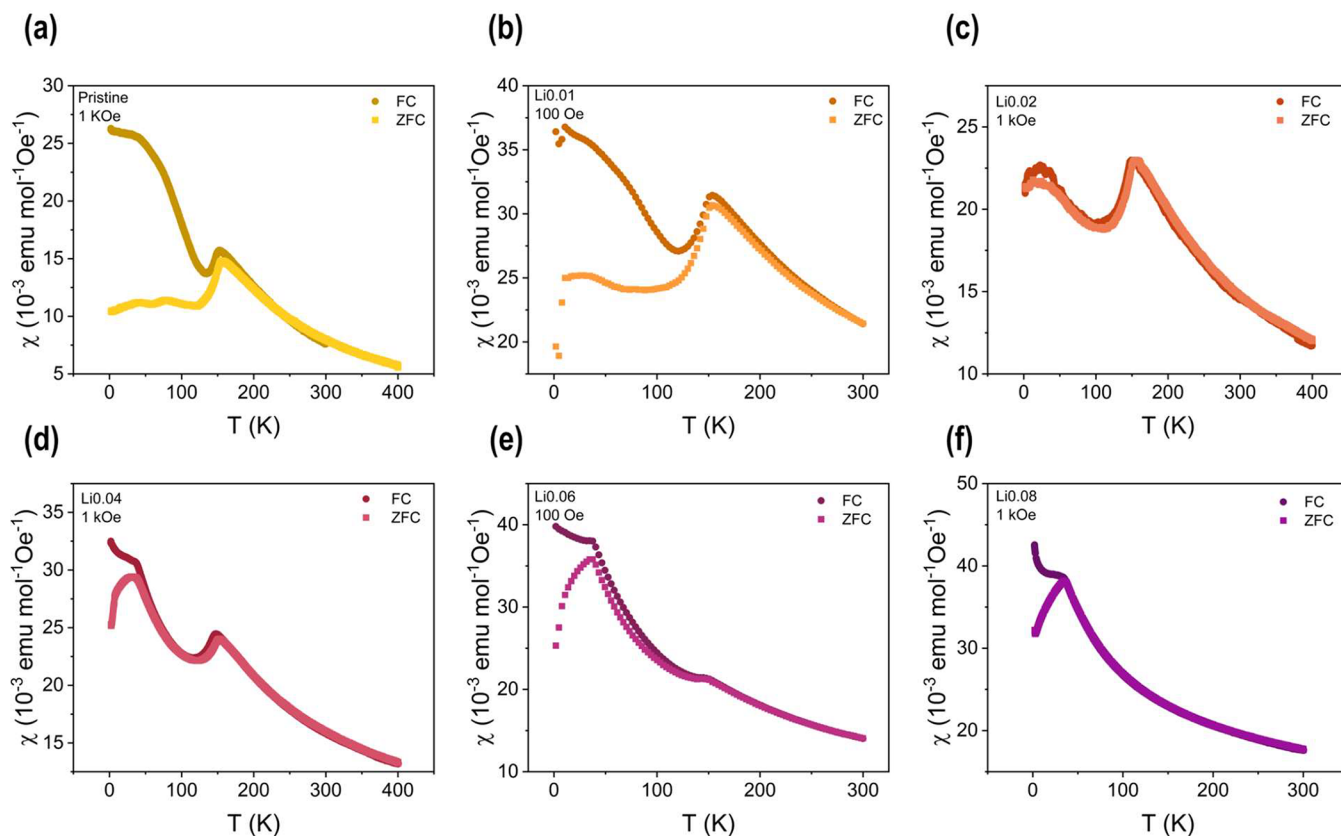


Figure 4. DC magnetic susceptibilities of (a) pristine $\text{Fe}_{1/4}\text{NbS}_2$, (b) $\text{Li}_{0.01}\text{Fe}_{1/4}\text{NbS}_2$, (c) $\text{Li}_{0.02}\text{Fe}_{1/4}\text{NbS}_2$, (d) $\text{Li}_{0.04}\text{Fe}_{1/4}\text{NbS}_2$, (e) $\text{Li}_{0.06}\text{Fe}_{1/4}\text{NbS}_2$, and (f) $\text{Li}_{0.08}\text{Fe}_{1/4}\text{NbS}_2$. All samples were slow-cooled.

Ex situ X-ray absorption spectroscopy (Figure S4) of all lithiated samples $\text{Li}_x\text{Fe}_{1/4}\text{NbS}_2$ ($x = 0-0.08$) revealed no shift in the Fe K-edge, which confirmed a constant and magnetically active Fe^{2+} oxidation state and that all electron transfer during lithiation must have occurred at Nb centers with d^1 partially filled orbitals near the Fermi level. DC-field magnetic susceptibility of the lithiation series under zero-field cooling (ZFC) and field cooling (FC) was measured from 300 K down to 2 K (Figure 4), and the Curie–Weiss fitting was performed on the high-temperature ZFC data (>200 K) above any long-range magnetic ordering temperature. Note that a field of 1 kOe or 100 Oe is used depending on whether the sample was measured in a PPMS or a more sensitive MPMS, respectively. The results are summarized in Table S4, and the Curie–Weiss analysis is presented in Figure S5. The average paramagnetic moment obtained is $5.27 \mu_{\text{B}}$ per Fe, which is very close to the $4.9 \mu_{\text{B}}$ expected for Fe^{2+} , as calculated by the Curie–Weiss paramagnetic moment using $g\sqrt{S(S+1)}$. Furthermore, the value of θ_{CW} generally becomes more negative as the Li content increases, indicating stronger AFM interactions. Our measured θ_{CW} values for pristine $\text{Fe}_{1/4}\text{NbS}_2$ and $\text{Li}_{0.08}\text{Fe}_{1/4}\text{NbS}_2$ are very close to those reported in the literature for $\text{Fe}_{1/4}\text{NbS}_2$ and $\text{Fe}_{1/3}\text{NbS}_2$.²¹ Because spin frustration and competing ground states in $\text{Fe}_{1/3}\text{NbS}_2$ may have contributed to its overall lower T_{N} , we expect that a degree of geometric frustration is also present in $\text{Li}_{0.08}\text{Fe}_{1/4}\text{NbS}_2$, resulting in its similarly low T_{N} .

DC magnetic susceptibility measurements revealed two major features at 35 and 150 K. In the unlithiated state, a single AFM transition was observed at 150 K, consistent with the

Néel temperature (137–151 K) of pure $\text{Fe}_{1/4}\text{NbS}_2$ in the literature.^{21,42} The divergence between the ZFC and FC curves at low temperatures suggests a spin glass state or domain wall movement. The unusual upturn in magnetic susceptibility below T_{N} has previously been reported for $\text{Fe}_{1/4}\text{NbS}_2$, but its origin remains open.²¹ As the Li content increases, a clear trend arises in the magnetic susceptibility in which the 35 K feature continuously grows and the 150 K feature dampens. For $x = 0.04, 0.06$, and 0.08 , a significant divergence between ZFC and FC was also observed below the lower-temperature AFM transition. Once the Li content reaches $x = 0.08$, the only AFM transition present was at 35 K, close to the 45 K Néel temperature of pure $\text{Fe}_{1/3}\text{NbS}_2$. For $x = 0.04, 0.06$, and 0.08 , a significant divergence between ZFC and FC was also observed below 35 K. Note that the specific Néel temperature of $\text{Fe}_{1/3}\text{NbS}_2$ can change by up to 10 K, resulting from small deviations in Fe stoichiometry.³⁴ The two magnetic susceptibility features are likely associated with 2×2 and $\sqrt{3} \times \sqrt{3}$ Fe-ordered domains whose relative prevalence depends on the degree of lithium intercalation and, in turn, determines how strongly each Néel temperature is expressed. The transition resulting from lithiation is therefore first-order in nature instead of a solid solution. In other words, the gradual lithiation of $\text{Fe}_{1/4}\text{NbS}_2$ leads to the nucleation and growth of $\text{Li}_{1/12}\text{Fe}_{1/4}\text{NbS}_2$ in the $\text{Fe}_{1/4}\text{NbS}_2$ matrix. Note that the first-order transition we refer to here is not induced by a temperature change and therefore does not have a latent heat. In the lithiated domains, the nearest Fe–Fe distance is the same as that in $\text{Fe}_{1/3}\text{NbS}_2$, resulting in the much-reduced Néel temperature based on the RKKY exchange mechanism.

$\text{Li}_{0.08}\text{Fe}_{0.25}\text{NbS}_2$ has a lower electron doping level than $\text{Fe}_{0.33}\text{NbS}_2$ because of the different oxidation states of Li^+ and Fe^{2+} . Previous literature has noted that, in Fe_xNbS_2 , once $x > 0.25$, the Fe occupancy quickly adopts a $(\sqrt{3} \times \sqrt{3})$ -type ordering at $0.27 < x < 0.5$.^{65,66} Meanwhile, magnetic properties, measured in a narrower range of $0.30 < x < 0.35$, all showed highly similar AFM transitions at 40–45 K, among which $\text{Fe}_{0.30}\text{NbS}_2$ (with a reported $T_N = 45$ K) is almost isoelectronic with $\text{Li}_{0.08}\text{Fe}_{0.25}\text{NbS}_2$.^{34,67} Therefore, it appears that the Fe–Fe distance dominates the magnetic interaction type and intensity, whereas the effect of Fermi vector variation is small.

The deviation between the ZFC and FC curves at low magnetic fields suggests the presence of irreversibility in domain wall movement or spin glass. To gain further insight into this behavior, ac susceptibility measurements were carried out at different frequencies. The real part of the AC magnetic susceptibility (χ') as a function of the temperature at various frequencies is presented in Figure S6. The ac susceptibility results show that the transition temperature at 150 K does not change when the excitation frequency is varied. While there is no apparent departure to the onset of the 35 K transition, a small kink is observed in the $\chi'(T)$ curve at around 25 K. This result is indicative of irreversible magnetic domain movement rather than a glassy state. This is consistent with the A-type AFM magnetic ground state of the pristine material and the observation of different Fe-ordering domains [(2 × 2)-type and $(\sqrt{3} \times \sqrt{3})$ -type] associated with the level of lithium intercalation. The absence of a spin glass phase in the lithiated $\text{Li}_{1/12}\text{Fe}_{1/4}\text{NbS}_2$ phase ($x = 0.08$) stands in contrast to $\text{Fe}_{1/3\pm\delta}\text{NbS}_2$,⁶⁰ whose spin-glass texture was believed to give rise to the low-current electrical switching.³⁴ In $\text{Li}_{1/12}\text{Fe}_{1/4}\text{NbS}_2$, the average occupancy of the $\sqrt{3} \times \sqrt{3}$ Fe sublattice is only 75%, which disrupts a perfect $\sqrt{3} \times \sqrt{3}$ Fe order and might lift the necessary geometric frustration condition for a spin glass.

Synchrotron XRD was performed to confirm the presence of distinct coexisting Fe-ordering domains (Figure 5a). The primary differences between samples arose in the region between 1.5° and 4.5° (Figure 5b). The black and green ticks underneath the patterns mark the Bragg positions unique to the Fe orderings in a 2 × 2 superlattice and a $\sqrt{3} \times \sqrt{3}$ superlattice. While we observed only (2 × 2)-type superlattice peaks in pure $\text{Fe}_{1/4}\text{NbS}_2$, as the lithiation increases, peaks characteristic of the $(\sqrt{3} \times \sqrt{3})$ -type superlattice evolve and coexist until high lithiation contents, where only the $(\sqrt{3} \times \sqrt{3})$ -type superlattice peaks remain. Rietveld refinement (Figure S7) of each sample revealed the phase fractions and domain sizes, which are listed in Table S5. The refinement was based on the existence of two phases with distinct Fe ordering, i.e., an $\text{Fe}_{1/4}\text{NbS}_2$ phase with the 2 × 2 superlattice and an $\text{Fe}_{1/3}\text{NbS}_2$ phase with the $(\sqrt{3} \times \sqrt{3})$ -type superlattice and partial Fe occupancy of 75.8% (such that the overall Fe content remains $1/4$ per f.u.). Based on the refinement, the phase fraction changes proportionally to the Li content, with exclusively (2 × 2)-type Fe ordering in pristine $\text{Fe}_{1/4}\text{NbS}_2$ and mostly $(\sqrt{3} \times \sqrt{3})$ -type ordering (~90%) in $\text{Li}_{0.08}\text{Fe}_{1/4}\text{NbS}_2$ (schematic shown in Figure 5c), which agrees with the relative predominance of the two AFM transitions in magnetization. The domain sizes refined are on a several-hundred-nanometer scale, indicating a first-order bulk phase separation between the two coexisting phases.

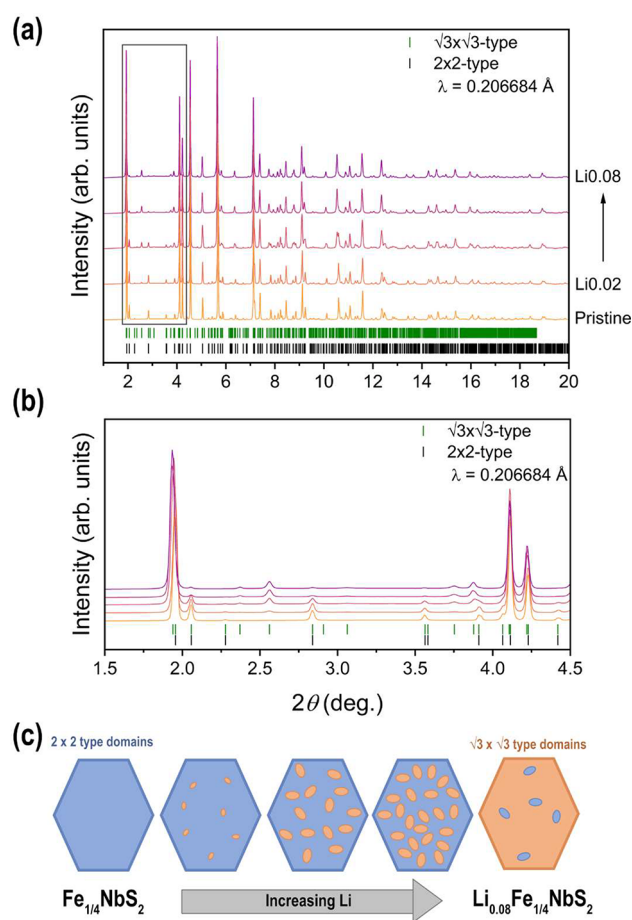


Figure 5. (a) Synchrotron XRD patterns of the lithiation series (pristine $\text{Fe}_{1/4}\text{NbS}_2$ and $\text{Li}_x\text{Fe}_{1/4}\text{NbS}_2$ at $x = 0.02, 0.04, 0.06, 0.08$), all annealed and slow-cooled. The gray box from 1.5 to 4.5° highlights the region where low-intensity peaks differentiate the (2 × 2)-type and $(\sqrt{3} \times \sqrt{3})$ -type Fe site order. (b) Magnification of the 1.5–4.5° region. (c) Schematic of the (2 × 2)-type and $(\sqrt{3} \times \sqrt{3})$ -type Fe-ordered domain distributions as a function of lithiation.

SEM–EDS was performed and is shown in Figure S8a,b for slow-cooled $\text{Li}_{0.08}\text{Fe}_{1/4}\text{NbS}_2$. Fe was observed to distribute homogeneously across particles or within individual particles, thereby ruling out the possibility of macroscopic Li or Fe segregation. However, it is still possible that such Li-rich or Fe-rich domains exist in the short range. We further examine this possibility using the PDF data obtained by Fourier transform infrared (FTIR) its synchrotron diffraction pattern in Figure 5a. We compared two models with and without local Li/Fe segregation (Figure S8c,d and Tables S6 and S7). We found that both models provide similar refinement and thus could not conclusively conclude whether there is local Li segregation.

Thermal-History-Dependent Fe Site Order. The coexistence of minor $(\sqrt{3} \times \sqrt{3})$ -type order within a (2 × 2)-type matrix in vapor-transport-grown $\text{Fe}_{1/4}\text{NbS}_2$ crystals has previously been observed through dark-field transmission electron microscopy (TEM) imaging.⁶⁶ The $(\sqrt{3} \times \sqrt{3})$ -characteristic diffraction spots became more intense during in situ heating to above 600 K inside a TEM chamber and were frozen-in by fast cooling,⁶⁶ with the domain size depending on the cooling rate. In this original study, the authors suggest that the transformation from long linear Fe–Nb chains along *c* characteristic of the 2 × 2 superlattice to staggered Nb–Fe–

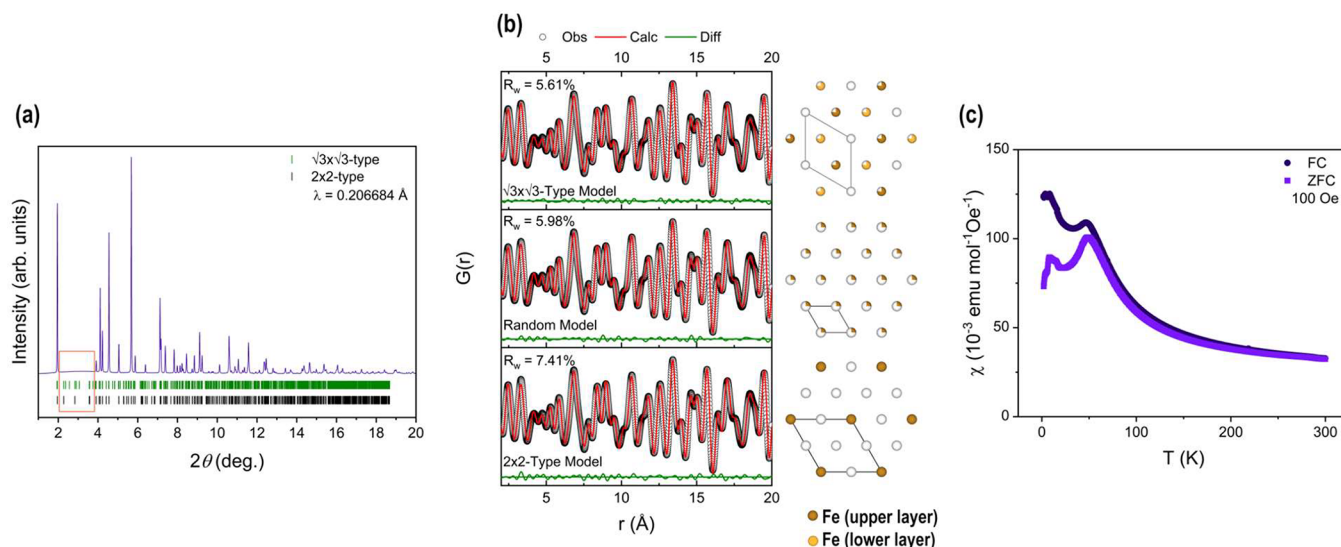


Figure 6. (a) Synchrotron XRD pattern of water-quenched $\text{Fe}_{1/4}\text{NbS}_2$. The orange box highlights the characteristic superlattice peaks that are featureless. (b) PDF fits in low interatomic distances (2–20 Å). Organized top to bottom are the $(\sqrt{3} \times \sqrt{3})$ -type, random, and (2×2) -type ordered models. (c) dc magnetic susceptibility of water-quenched $\text{Fe}_{1/4}\text{NbS}_2$.

Nb chains in the $\sqrt{3} \times \sqrt{3}$ superlattice allows the structure to better accommodate thermal vibrations at high temperatures.⁶⁶ The thermal history dependence of domain ordering and size in pristine $\text{Fe}_{1/4}\text{NbS}_2$ suggests a second method to modify the Fe site order and, thus, magnetic properties.

To further explore the thermal-history dependence, we annealed pristine $\text{Fe}_{1/4}\text{NbS}_2$ at 400 °C in a vacuum-sealed quartz ampule for 18 h before water quenching the sample. Synchrotron XRD (Figure 6a) revealed that none of the characteristic low-intensity peaks between 1.5° and 4.5° were present, a significant departure from the slow-cooled pristine or slow-cooled lithiated samples discussed earlier. The lack of characteristic low-intensity peaks is likely the result of a significant decrease in the coherent length on the order of the Fe intercalants. Thus, a Fourier transform was applied to the diffraction data to obtain and fit the pair distribution function (PDF) over short interatomic distances (2–20 Å). Three different structural models for Fe site order, i.e., (2×2) -type with full Fe occupancy, $(\sqrt{3} \times \sqrt{3})$ -type with partial Fe occupancy, and completely random with equal partial Fe occupancy in all octahedral sites in the layer, were fit to the data (Figure 6b), and the resulting fitting parameters are presented in Tables S8–S10. It was found that the $(\sqrt{3} \times \sqrt{3})$ -type ordering had the best fit ($R_w = 5.56\%$); however, the random ordering was very close ($R_w = 5.93\%$). This suggests dominant $(\sqrt{3} \times \sqrt{3})$ -type Fe ordering with nanoscale domain sizes and border regions containing significant Fe disorder. This hypothesis is reinforced by the sole magnetic susceptibility feature characteristic to $(\sqrt{3} \times \sqrt{3})$ -type Fe ordering, i.e., a Néel temperature at 45 K (Figure 6c).

Combining lithiation and quenching does not further change the magnetic susceptibility, as shown in Figure S9. Only one AFM ordering temperature was observed at ~ 41 K for water-quenched $\text{Li}_x\text{Fe}_{1/4}\text{NbS}_2$ at both $x = 0.09$ and 0.14, suggesting dominant $(\sqrt{3} \times \sqrt{3})$ -type Fe site order in these samples. Magnetization as a function of the field strength was measured at 1.8, 20, and 50 K for $x = 0.14$ (Figure S9). A linear response without hysteresis was observed for 20 K and above, consistent with the AFM state. The small hysteresis observed at 1.8 K is similar to that in $\text{Fe}_{1/3}\text{NbS}_2$, which was attributed to a spin

glass state.²⁹ Because we have excluded the possibility of a spin glass with frequency-independent magnetic susceptibility, the observed hysteresis might arise from the occupation disorder of Fe.

CONCLUSIONS

In summary, through neutron powder diffraction, we determined the magnetic ground state of $\text{Fe}_{1/4}\text{NbS}_2$ to be an A-type antiferromagnet with out-of-plane moments from high-spin-state Fe^{2+} ($S = 2$). Despite the presence of overall inversion symmetry, the compound has spin polarization induced by AFM order at generic k points, as confirmed by DFT calculations, thus constituting one example that manifests the new nonrelativistic spin-polarization effect. Given the dominant RKKY exchange mechanism and its oscillatory nature, tuning of the Fe site order was explored by electrochemical lithiation and thermal history. Overall, we did not find an intermediate Fe order type between those of $\text{Fe}_{1/4}\text{NbS}_2$ and $\text{Fe}_{1/3}\text{NbS}_2$. The intercalation of Li ions as nonmagnetic spacers in $\text{Fe}_{1/4}\text{NbS}_2$ leads to a first-order phase transition from (2×2) -type to $(\sqrt{3} \times \sqrt{3})$ -type Fe order with 100-nm domain sizes, as confirmed by synchrotron diffraction, whereas quenching instead of slow cooling favors the development of short-range $(\sqrt{3} \times \sqrt{3})$ -type Fe order based on PDF analysis. Combining magnetic susceptibility measurements, we determine that the overall phase fraction of each Fe ordering type determines the relative dominance of the magnetic feature expressed at the respective Néel temperatures. A subtle difference was observed between the $x(\text{Li}) = 0.08$ per f.u. of lithiated $\text{Fe}_{1/4}\text{NbS}_2$ and $\text{Fe}_{1/3}\text{NbS}_2$ despite the same number of total intercalants and $(\sqrt{3} \times \sqrt{3})$ -type Fe order. Unlike the latter, the bifurcation in ZFC and FC susceptibility of the former originates from irreversible domain wall movement instead of a spin-glass phase, which we tentatively attribute to the disruption of local triangular cooccupation of Fe by Li.

■ ASSOCIATED CONTENT**SI Supporting Information**

The Supporting Information is available free of charge at <https://pubs.acs.org/doi/10.1021/acs.inorgchem.3c02652>.

Supplementary Notes 1 and 2; Supplementary Figures S1–S9, including single crystal, ac, and quenched-powder magnetization measurements, DFT-calculated strain effect, lithiation voltage profiles, X-ray absorption spectra, Curie–Weiss fitting, Rietveld refinements, and SEM results, and Supplementary Tables S1–S10, including crystallographic information and refinement parameters, Curie–Weiss fitting parameters, and DFT energies (PDF)

■ AUTHOR INFORMATION**Corresponding Author**

Huiwen Ji – Department of Materials Science and Engineering, University of Utah, Salt Lake City, Utah 84112, United States; Email: huiwen.ji@utah.edu

Authors

Erick A. Lawrence – Department of Materials Science and Engineering, University of Utah, Salt Lake City, Utah 84112, United States; orcid.org/0000-0003-0819-1895

Xudong Huai – Department of Chemistry, Clemson University, Clemson, South Carolina 29634, United States

Dongwook Kim – Department of Materials Science and Engineering, University of Utah, Salt Lake City, Utah 84112, United States

Maxim Avdeev – Australian Centre for Neutron Scattering, Australian Nuclear Science and Technology Organization, Kirrawee DC, New South Wales 2232, Australia; School of Chemistry, University of Sydney, Sydney, New South Wales 2006, Australia; orcid.org/0000-0003-2366-5809

Yu Chen – Department of Materials Science and Engineering, University of California Berkeley, Berkeley, California 94720, United States; Materials Sciences Division, Lawrence Berkeley National Laboratory, Berkeley, California 94720, United States; orcid.org/0000-0002-5420-7571

Grigorii Skorupskii – Department of Chemistry, Princeton University, Princeton, New Jersey 08544, United States

Akira Miura – Graduate School of Engineering, Hokkaido University, Sapporo, Hokkaido 8628, Japan; orcid.org/0000-0003-0388-9696

Austin Ferrenti – Department of Chemistry, Johns Hopkins University, Baltimore, Maryland 21218, United States; orcid.org/0000-0003-2075-9041

Moritz Waibel – Department of Materials Science and Engineering, University of Utah, Salt Lake City, Utah 84112, United States; Faculty of Physics, Ludwig-Maximilians-University, Munich, Bavaria 80539, Germany

Shogo Kawaguchi – Japan Synchrotron Radiation Research Institute, Hyogo 679-5198, Japan

Nicholas Ng – Department of Chemistry, Johns Hopkins University, Baltimore, Maryland 21218, United States

Bobby Kaman – Department of Materials Science and Engineering, University of Utah, Salt Lake City, Utah 84112, United States; Department of Materials Science and Engineering, University of Illinois Urbana–Champaign, Champaign, Illinois 61820, United States

Zijian Cai – Department of Materials Science and Engineering, University of California Berkeley, Berkeley, California 94720,

United States; Materials Sciences Division, Lawrence Berkeley National Laboratory, Berkeley, California 94720, United States; orcid.org/0000-0002-4908-3180

Leslie Schoop – Department of Chemistry, Princeton University, Princeton, New Jersey 08544, United States; orcid.org/0000-0003-3459-4241

Satya Kushwaha – Department of Chemistry, Johns Hopkins University, Baltimore, Maryland 21218, United States

Feng Liu – Department of Materials Science and Engineering, University of Utah, Salt Lake City, Utah 84112, United States; orcid.org/0000-0002-3701-8058

Thao T. Tran – Department of Chemistry, Clemson University, Clemson, South Carolina 29634, United States; orcid.org/0000-0002-2395-3555

Complete contact information is available at:

<https://pubs.acs.org/doi/10.1021/acs.inorgchem.3c02652>

Notes

The authors declare no competing financial interest.

■ ACKNOWLEDGMENTS

Research performed at the University of Utah was supported by National Science Foundation (NSF) Grant 2145832. The computational work was supported by U.S. Department of Energy (DOE), Basic Energy Sciences (Grant DE-FG02-04ER46148). Support from the CHPC at the University of Utah and the NERSC at the Office of Science in the U.S. DOE is gratefully acknowledged. X.H. and T.T.T. thank the NSF (OIA-2227933) for support. Synchrotron XRD measurements were approved by Japan Synchrotron Radiation Research Institute (JASRI) with the approved number of 2023A1042. A.M. thanks Dr. Kawaguchi Shogo (JASRI) and Prof. Chikako Moriyoshi (Hiroshima University) for synchrotron XRD measurements. This work was partially supported by KAKENHI JP20KK0124. The MPMS3 system used for magnetic characterization was funded by the NSF, Division of Materials Research, Major Research Instrumentation Program, under Grant 1828490. This work also made use of the University of Utah shared facilities of the Micron Technology Foundation Inc. Microscopy Suite sponsored by the John and Marcia Price College of Engineering, Health Sciences Center, Office of the Vice President for Research. The work at Princeton University was supported by the Gordon and Betty Moore Foundation's EPIQS Initiative (grant number GBMF9064), the Princeton Catalysis Initiative (PCI), the David and Lucille Packard Foundation and the Arnold and Mabel Beckman foundation through a BYI grant to L.M.S. and an Arnold O. Beckman postdoctoral fellowship to G.S. This material is based on work supported by the NSF-MIP Platform for the Accelerated Realization, Analysis, and Discovery of Interface Materials (PARADIM) under Cooperative Agreement DMR-2039380.

■ REFERENCES

- (1) Morosan, E.; Zandbergen, H. W.; Dennis, B.; Bos, J.; Onose, Y.; Klimczuk, T.; Ramirez, A.; Ong, N.; Cava, R. J. Superconductivity in Cu x TiSe2. *Nat. Phys.* **2006**, *2* (8), 544–550.
- (2) Luo, H.; Xie, W.; Tao, J.; Inoue, H.; Gyenis, A.; Krizan, J. W.; Yazdani, A.; Zhu, Y.; Cava, R. J. Polytypism, polymorphism, and superconductivity in TaSe_{2-x}Te_x. *Proc. Natl. Acad. Sci. U. S. A.* **2015**, *112* (11), E1174–E1180.
- (3) Valla, T.; Fedorov, A.; Johnson, P.; Glans, P.; McGuinness, C.; Smith, K.; Andrei, E.; Berger, H. Quasiparticle Spectra, Charge-

- Density Waves, Superconductivity, and Electron-Phonon Coupling in 2 H– Nb S e 2. *Physical review letters* **2004**, *92* (8), No. 086401.
- (4) Wagner, K.; Morosan, E.; Hor, Y.; Tao, J.; Zhu, Y.; Sanders, T.; McQueen, T.; Zandbergen, H.; Williams, A.; West, D.; Cava, R. Tuning the charge density wave and superconductivity in Cu_xTaS_2 . *Phys. Rev. B* **2008**, *78* (10), No. 104520.
- (5) Arguello, C. J.; Rosenthal, E. P.; Andrade, E. F.; Jin, W.; Yeh, P.; Zaki, N.; Jia, S.; Cava, R. J.; Fernandes, R. M.; Millis, A. J.; Valla, T.; Osgood, R. M.; Pasupathy, A. N. Quasiparticle Interference, Quasiparticle Interactions, and the Origin of the Charge Density Wave in 2 H– NbSe 2. *Physical review letters* **2015**, *114* (3), No. 037001.
- (6) Arguello, C. J.; Chockalingam, S. P.; Rosenthal, E. P.; Zhao, L.; Gutiérrez, C.; Kang, J.; Chung, W.; Fernandes, R. M.; Jia, S.; Millis, A. J.; Cava, R. J.; Pasupathy, A. N. Visualizing the charge density wave transition in 2 H– NbSe 2 in real space. *Phys. Rev. B* **2014**, *89* (23), No. 235115.
- (7) Ali, M. N.; Xiong, J.; Flynn, S.; Tao, J.; Gibson, Q. D.; Schoop, L. M.; Liang, T.; Haldolaarachchige, N.; Hirschberger, M.; Ong, N. P.; Cava, R. J. Large, non-saturating magnetoresistance in WTe_2 . *Nature* **2014**, *514* (7521), 205–208.
- (8) Guguchia, Z.; von Rohr, F.; Shermadini, Z.; Lee, A. T.; Banerjee, S.; Wieteska, A.; Marianetti, C.; Frandsen, B.; Luetkens, H.; Gong, Z.; Cheung, S. C.; Baines, C.; Shengelaya, A.; Taniashvili, G.; Pasupathy, A. N.; Morenzoni, E.; Billinge, S. J. L.; Amato, A.; Cava, R. J.; Khasanov, R.; Uemura, Y. J. Signatures of the topological $s+$ –superconducting order parameter in the type-II Weyl semimetal Td-MoTe_2 . *Nat. Commun.* **2017**, *8* (1), 1082.
- (9) Qian, X.; Liu, J.; Fu, L.; Li, J. Quantum spin Hall effect in two-dimensional transition metal dichalcogenides. *Science* **2014**, *346* (6215), 1344–1347.
- (10) Xie, L. S.; Husremovic, S.; Gonzalez, O.; Craig, I. M.; Bediako, D. K. Structure and Magnetism of Iron-and Chromium-Intercalated Niobium and Tantalum Disulfides. *J. Am. Chem. Soc.* **2022**, *144* (22), 9525–9542.
- (11) Manzeli, S.; Ovchinnikov, D.; Pasquier, D.; Yazyev, O. V.; Kis, A. 2D transition metal dichalcogenides. *Nat. Rev. Mater.* **2017**, *2* (8), 1–15.
- (12) Hulliger, F.; Pobitschka, E. On the magnetic behavior of new 2H– NbS2-type derivatives. *J. Solid State Chem.* **1970**, *1* (2), 117–119.
- (13) Van Laar, B.; Rietveld, H.; Ijdo, D. Magnetic and crystallographic structures of MexNbS_2 and MexTaS_2 . *J. Solid State Chem.* **1971**, *3* (2), 154–160.
- (14) Fan, S.; Zou, X.; Du, H.; Gan, L.; Xu, C.; Lv, W.; He, Y.-B.; Yang, Q.-H.; Kang, F.; Li, J. Theoretical investigation of the intercalation chemistry of lithium/sodium ions in transition metal dichalcogenides. *J. Phys. Chem. C* **2017**, *121* (25), 13599–13605.
- (15) Xiong, F.; Wang, H.; Liu, X.; Sun, J.; Brongersma, M.; Pop, E.; Cui, Y. Li intercalation in MoS_2 : in situ observation of its dynamics and tuning optical and electrical properties. *Nano Lett.* **2015**, *15* (10), 6777–6784.
- (16) Jung, Y.; Zhou, Y.; Cha, J. J. Intercalation in two-dimensional transition metal chalcogenides. *Inorganic Chemistry Frontiers* **2016**, *3* (4), 452–463.
- (17) Wang, N.; Tang, H.; Shi, M.; Zhang, H.; Zhuo, W.; Liu, D.; Meng, F.; Ma, L.; Ying, J.; Zou, L.; Sun, Z.; Chen, X. Transition from ferromagnetic semiconductor to ferromagnetic metal with enhanced Curie temperature in $\text{Cr}_2\text{Ge}_2\text{Te}_6$ via organic ion intercalation. *J. Am. Chem. Soc.* **2019**, *141* (43), 17166–17173.
- (18) Wilson, J. A.; Yoffe, A. The transition metal dichalcogenides discussion and interpretation of the observed optical, electrical and structural properties. *Adv. Phys.* **1969**, *18* (73), 193–335.
- (19) Marseglia, E. Transition metal dichalcogenides and their intercalates. *Int. Rev. Phys. Chem.* **1983**, *3* (2), 177–216.
- (20) Anzenhofer, K.; Van Den Berg, J.; Cossee, P.; Helle, J. The crystal structure and magnetic susceptibilities of MnNb_3S_6 , FeNb_3S_6 , CoNb_3S_6 and NiNb_3S_6 . *J. Phys. Chem. Solids* **1970**, *31* (5), 1057–1067.
- (21) Gorochoy, O.; Blanc-soreau, A. L.; Rouxel, J.; Imbert, P.; Jehanno, G. Transport properties, magnetic susceptibility and Mössbauer spectroscopy of FeO . 25NbS_2 and FeO . 33NbS_2 . *Philosophical Magazine B* **1981**, *43* (4), 621–634.
- (22) Yamamura, Y.; Moriyama, S.; Tsuji, T.; Iwasa, Y.; Koyano, M.; Katayama, S. i.; Ito, M. Heat capacity and phase transition of Fe_xNbS_2 at low temperature. *Journal of alloys and compounds* **2004**, *383* (1–2), 338–341.
- (23) Yoshioka, T.; Tazuke, Y. Magnetic Properties of Fe_xTiS_2 System. *J. Phys. Soc. Jpn.* **1985**, *54* (6), 2088–2091.
- (24) Pleschov, V.; Baranov, N.; Titov, A.; Inoue, K.; Bartashevich, M.; Goto, T. Magnetic properties of Cr-intercalated TiSe_2 . *Journal of alloys and compounds* **2001**, *320* (1), 13–17.
- (25) Tazuke, Y.; Takeyama, T. Magnetic Properties of 3d Transition Element Intercalated Compounds M_xTiSe_2 . *J. Phys. Soc. Jpn.* **1997**, *66* (3), 827–830.
- (26) Erodici, M. P.; Mai, T. T.; Xie, L. S.; Li, S.; Fender, S. S.; Husremović, S.; Gonzalez, O.; Hight Walker, A. R.; Bediako, D. K. Bridging Structure, Magnetism, and Disorder in Iron-Intercalated Niobium Diselenide, Fe_xNbSe_2 , below $x = 0.25$. *J. Phys. Chem. C* **2023**, *127*, 9787.
- (27) Koski, K. J.; Wessells, C. D.; Reed, B. W.; Cha, J. J.; Kong, D.; Cui, Y. Chemical intercalation of zerovalent metals into 2D layered Bi_2Se_3 nanoribbons. *J. Am. Chem. Soc.* **2012**, *134* (33), 13773–13779.
- (28) Morosan, E.; Zandbergen, H.; Li, L.; Lee, M.; Checkelsky, J.; Heinrich, M.; Siegrist, T.; Ong, N. P.; Cava, R. Sharp switching of the magnetization in $\text{Fe}_{1/4}\text{TaS}_2$. *Phys. Rev. B* **2007**, *75* (10), No. 104401.
- (29) Nair, N. L.; Maniv, E.; John, C.; Doyle, S.; Orenstein, J.; Analytis, J. G. Electrical switching in a magnetically intercalated transition metal dichalcogenide. *Nature materials* **2020**, *19* (2), 153–157.
- (30) Miyadai, T.; Kikuchi, K.; Kondo, H.; Sakka, S.; Arai, M.; Ishikawa, Y. Magnetic properties of $\text{Cr}_{1/3}\text{NbS}_2$. *J. Phys. Soc. Jpn.* **1983**, *52* (4), 1394–1401.
- (31) Zhang, C.; Zhang, J.; Liu, C.; Zhang, S.; Yuan, Y.; Li, P.; Wen, Y.; Jiang, Z.; Zhou, B.; Lei, Y.; Zheng, D.; Song, C.; Hou, Z.; Mi, W.; Schwingenschlög, U.; Manchon, A.; Qiu, Z. Q.; Alshareef, H. N.; Peng, Y.; Zhang, X.-X. Chiral Helimagnetism and One-Dimensional Magnetic Solitons in a Cr-Intercalated Transition Metal Dichalcogenide. *Adv. Mater.* **2021**, *33* (35), No. 2101131.
- (32) Wadley, P.; Howells, B.; Železný, J.; Andrews, C.; Hills, V.; Campion, R. P.; Novák, V.; Olejník, K.; Maccheronzi, F.; Dhesi, S.; et al. Electrical switching of an antiferromagnet. *Science* **2016**, *351* (6273), 587–590.
- (33) Bodnar, S. Y.; Šmejkal, L.; Turek, I.; Jungwirth, T.; Gomonay, O.; Sinova, J.; Sapozhnik, A.; Elmers, H.-J.; Kläui, M.; Jourdan, M. Writing and reading antiferromagnetic Mn_2Au by Néel spin-orbit torques and large anisotropic magnetoresistance. *Nat. Commun.* **2018**, *9* (1), 348.
- (34) Wu, S.; Xu, Z.; Haley, S. C.; Weber, S. F.; Acharya, A.; Maniv, E.; Qiu, Y.; Aczel, A.; Settineri, N. S.; Neaton, J. B.; Analytis, J. G.; Birgeneau, R. J. Highly Tunable Magnetic Phases in Transition-Metal Dichalcogenide $\text{Fe}_{1/3+\delta}\text{NbS}_2$. *Physical Review X* **2022**, *12* (2), No. 021003.
- (35) Parkin, S.; Friend, R. 3 d transition-metal intercalates of the niobium and tantalum dichalcogenides. I. Magnetic properties. *Philosophical Magazine B* **1980**, *41* (1), 65–93.
- (36) Parkin, S.; Friend, R. 3 d transition-metal intercalates of the niobium and tantalum dichalcogenides. II. Transport properties. *Philosophical Magazine B* **1980**, *41* (1), 95–112.
- (37) Ko, K.-T.; Kim, K.; Kim, S. B.; Kim, H.-D.; Kim, J.-Y.; Min, B.; Park, J.-H.; Chang, F.-H.; Lin, H.-J.; Tanaka, A.; Cheong, S.-W. RKKY ferromagnetism with ising-like spin states in intercalated $\text{Fe}_{1/4}\text{TaS}_2$. *Physical review letters* **2011**, *107* (24), No. 247201.
- (38) Du, K.; Huang, F.-T.; Kim, J.; Lim, S. J.; Gamage, K.; Yang, J.; Mostovoy, M.; Garlow, J.; Han, M.-G.; Zhu, Y.; Cheong, S.-W. Topological spin/structure couplings in layered chiral magnet CrI_2

- 3TaS₂: The discovery of spiral magnetic superstructure. *Proc. Natl. Acad. Sci. U. S. A.* **2021**, *118* (40), No. e2023337118.
- (39) Togawa, Y.; Koyama, T.; Takayanagi, K.; Mori, S.; Kousaka, Y.; Akimitsu, J.; Nishihara, S.; Inoue, K.; Ovchinnikov, A.; Kishine, J.-i. Chiral magnetic soliton lattice on a chiral helimagnet. *Physical review letters* **2012**, *108* (10), No. 107202.
- (40) Zhang, X.; Liu, Q.; Luo, J.-W.; Freeman, A. J.; Zunger, A. Hidden spin polarization in inversion-symmetric bulk crystals. *Nat. Phys.* **2014**, *10* (5), 387–393.
- (41) Yuan, L.-D.; Wang, Z.; Luo, J.-W.; Zunger, A. Prediction of low-Z collinear and noncollinear antiferromagnetic compounds having momentum-dependent spin splitting even without spin-orbit coupling. *Physical Review Materials* **2021**, *5* (1), No. 014409.
- (42) Tsuji, T.; Yamamura, Y.; Koyano, M.; Katayama, S. i.; Ito, M. Thermodynamic and magnetic properties of intercalated layered compounds Fe_xNbS₂. *Journal of alloys and compounds* **2001**, *317*, 213–216.
- (43) Mangelsen, S.; Hansen, J.; Adler, P.; Schnelle, W.; Bensch, W.; Mankovsky, S.; Polesya, S.; Ebert, H. Large Anomalous Hall Effect and Slow Relaxation of the Magnetization in Fe_{1/3}TaS₂. *J. Phys. Chem. C* **2020**, *124* (45), 24984–24994.
- (44) Le Blanc-Soreau, A.; Rouxel, J.; Gardette, M.-F.; Gorochov, O. Propriétés électriques et magnétiques de MnO, 25NbS₂ et MnO, 33NbS₂. *Mater. Res. Bull.* **1976**, *11* (9), 1061–1071.
- (45) Avdeev, M.; Hester, J. R. ECHIDNA: a decade of high-resolution neutron powder diffraction at OPAL. *J. Appl. Crystallogr.* **2018**, *51* (6), 1597–1604.
- (46) Larson, A. C.; Von Dreele, R. B. *Gsas. Report IAU*, 1994; pp 86–748.
- (47) Toby, B. H. EXPGUI, a graphical user interface for GSAS. *Journal of applied crystallography* **2001**, *34* (2), 210–213.
- (48) Yang, X.; Juhas, P.; Farrow, C. L.; Billinge, S. J. xPDFsuite: an end-to-end software solution for high throughput pair distribution function transformation, visualization and analysis. *arXiv preprint arXiv:1402.3163* 2014.
- (49) Farrow, C.; Juhas, P.; Liu, J.; Bryndin, D.; Božin, E.; Bloch, J.; Proffen, T.; Billinge, S. PDFfit2 and PDFgui: computer programs for studying nanostructure in crystals. *J. Phys.: Condens. Matter* **2007**, *19* (33), No. 335219.
- (50) Kresse, G.; Furthmüller, J. Efficiency of ab-initio total energy calculations for metals and semiconductors using a plane-wave basis set. *Computational materials science* **1996**, *6* (1), 15–50.
- (51) Perdew, J. P.; Burke, K.; Ernzerhof, M. Generalized gradient approximation made simple. *Physical review letters* **1996**, *77* (18), 3865.
- (52) Monkhorst, H. J.; Pack, J. D. Special points for Brillouin-zone integrations. *Phys. Rev. B* **1976**, *13* (12), 5188.
- (53) Rouxel, J.; Leblanc, A.; Royer, A. Etude générale de systèmes MXNbS₂ (M élément de transition de la première période). *Bull. Soc. Chim. Fr.* **1971**, *6*, 2019–2022.
- (54) Perez-Mato, J.; Gallego, S.; Tasci, E.; Elcoro, L.; de la Flor, G.; Aroyo, M. Symmetry-based computational tools for magnetic crystallography. *Annu. Rev. Mater. Res.* **2015**, *45*, 217–248.
- (55) Spaldin, N. A. *Magnetic Materials: Fundamentals and Applications*; Cambridge University Press, 2010.
- (56) Lander, L.; Reynaud, M.; Rodríguez-Carvajal, J.; Tarascon, J.-M.; Rouse, G. Magnetic Structures of Orthorhombic Li₂M(SO₄)₂ (M= Co, Fe) and Li_xFe(SO₄)₂ (x= 1, 1.5) Phases. *Inorganic chemistry* **2016**, *55* (22), 11760–11769.
- (57) Yuan, L.-D.; Wang, Z.; Luo, J.-W.; Rashba, E. I.; Zunger, A. Giant momentum-dependent spin splitting in centrosymmetric low-Z antiferromagnets. *Phys. Rev. B* **2020**, *102* (1), No. 014422.
- (58) Bradley, C.; Cracknell, A. *The Mathematical Theory of Symmetry in Solids: Representation Theory for Point Groups and Space Groups*; Oxford University Press, 2010.
- (59) Šmejkal, L.; Sinova, J.; Jungwirth, T. Emerging research landscape of altermagnetism. *Physical Review X* **2022**, *12* (4), No. 040501.
- (60) Maniv, E.; Nair, N. L.; Haley, S. C.; Doyle, S.; John, C.; Cabrini, S.; Maniv, A.; Ramakrishna, S. K.; Tang, Y.-L.; Ercius, P.; et al. Antiferromagnetic switching driven by the collective dynamics of a coexisting spin glass. *Science advances* **2021**, *7* (2), No. eabd8452.
- (61) Li, Y.; Fuller, E. J.; Asapu, S.; Agarwal, S.; Kurita, T.; Yang, J. J.; Talin, A. A. Low-voltage, cmos-free synaptic memory based on li x tio2 redox transistors. *ACS Appl. Mater. Interfaces* **2019**, *11* (42), 38982–38992.
- (62) Cui, J.; Peng, H.; Song, Z.; Du, Z.; Chao, Y.; Chen, G. Significantly enhanced thermoelectric performance of γ-In₂Se₃ through lithiation via chemical diffusion. *Chem. Mater.* **2017**, *29* (17), 7467–7474.
- (63) Ying, T.; Gu, Y.; Chen, X.; Wang, X.; Jin, S.; Zhao, L.; Zhang, W.; Chen, X. Anderson localization of electrons in single crystals: Li x Fe₇Se₈. *Science advances* **2016**, *2* (2), No. e1501283.
- (64) Kobayashi, H.; Kanno, R.; Kawamoto, Y.; Tabuchi, M.; Nakamura, O. Physical properties of the de-lithiated Li₂- xRuO₃ with the layered structure. *Solid State Ionics* **1996**, *86*, 859–863.
- (65) Drábek, M.; Hybler, J. i.; Rieder, M.; Böhmová, V. The system Fe–Nb–S and its geological implications. *Canadian Mineralogist* **2010**, *48* (5), 1059–1068.
- (66) Boswell, F.; Prodan, A.; Vaughan, W.; Corbett, J. On the ordering of Fe atoms in Fe_xNbS₂. *physica status solidi (a)* **1978**, *45* (2), 469–481.
- (67) Tsuji, T.; Yamamura, Y.; Watanabe, H.; Saito, K.; Sorai, M. Heat capacity of intercalated layered materials Fe x NbS₂ at low temperature. *J. Therm. Anal. Calorim.* **1999**, *57* (3), 839–846.